*Article*

# Photocatalytic and Photo-Fenton Catalytic Degradation Activities of Z-Scheme Ag$_2$S/BiFeO$_3$ Heterojunction Composites under Visible-Light Irradiation

**Lijing Di [1,2], Hua Yang [1,*], Tao Xian [2,*], Xueqin Liu [3] and Xiujuan Chen [1]**

[1] State Key Laboratory of Advanced Processing and Recycling of Non-ferrous Metals, Lanzhou University of Technology, Lanzhou 730050, China; woshidilijing99@163.com (L.D.); chenxj@lut.cn (X.C.)

[2] College of Physics and Electronic Information Engineering, Qinghai Normal University, Xining 810008, China

[3] School of Science, Chongqing University of Technology, Chongqing 4000054, China; xqliu@cqut.edu.cn

[*] Correspondence: hyang@lut.cn (H.Y.); xiantao1204@163.com (T.X.); Tel.: +86-931-2973783 (H.Y.); +86-971-6307633 (T.X.)

**Abstract:** Z-scheme Ag$_2$S/BiFeO$_3$ heterojunction composites were successfully prepared through a precipitation method. The morphology and microstructure characterization demonstrate that Ag$_2$S nanoparticles (30–50 nm) are well-decorated on the surfaces of polyhedral BiFeO$_3$ particles (500–800 nm) to form Ag$_2$S/BiFeO$_3$ heterojunctions. The photocatalytic and photo-Fenton catalytic activities of the as-derived Ag$_2$S/BiFeO$_3$ heterojunction composites were evaluated by the degradation of methyl orange (MO) under visible-light irradiation. The photocatalytic result indicates that the Ag$_2$S/BiFeO$_3$ composites exhibit much improved photocatalytic activities when compared with bare Ag$_2$S and BiFeO$_3$. The optimum composite sample was observed to be 15% Ag$_2$S/BiFeO$_3$ with an Ag$_2$S mass fraction of 15%. Furthermore, the addition of H$_2$O$_2$ can further enhance the dye degradation efficiency, which is due to the synergistic effects of photo- and Fenton catalysis. The results of photoelectrochemical and photoluminescence measurements suggest a greater separation of the photoexcited electron/hole pairs in the Ag$_2$S/BiFeO$_3$ composites. According to the active species trapping experiments, the photocatalytic and photo-Fenton catalytic mechanisms of the Ag$_2$S/BiFeO$_3$ composites were proposed and discussed.

**Keywords:** polyhedral BiFeO$_3$ particles; Ag$_2$S nanoparticles; Z-scheme Ag$_2$S/BiFeO$_3$ heterojunction; photocatalysis; photo-Fenton catalysis

## 1. Introduction

Wastewater containing organic dyes or pigments has caused serious damage to environment and human health in recent times. Moreover, most of the organic pollutants are toxic, non-biodegradable, and are difficult to mineralize under natural conditions [1]. Several wastewater treatment routes have been used to eliminate organic pollutants from wastewater [2–10]. Compared with other elimination methods, advanced oxidation processes (AOPs) are demonstrated to be attractive methods for the efficient elimination of organic contaminants. In these processes, strong oxidizing radical species such as hydroxyl (•OH) radicals can be generated; they degrade most organic pollutants into innocuous byproducts [8,9]. Among various AOPs, photocatalytic and photo-Fenton-like catalytic processes have attracted remarkable attention for the decomposition of dyes, owing to their low cost, mild reaction

conditions, and easy operation procedures [11–19]. The photocatalysis process involves the generation of electron ($e^-$)-hole ($h^+$) pairs under suitable light irradiation, the transformation of photoexcited charges to the surface of photocatalyst, redox reactions of the charges with chemical species to form active species, and the degradation of pollutants by the attack of active species. The photo-Fenton-like catalytic process is based on the traditional Fenton process, and light irradiation. During the Fenton process, ●OH radicals can be derived from the reaction of the Fenton reagent [16–19]. During the Fenton reaction process, the introduction of additional light irradiation leads to the production of more ●OH radicals, which benefits from the synergistic effect between the photocatalysis and Fenton reactions [16–19]. However, the traditional photocatalysis and photo-Fenton-like catalytic processes are active only under the irradiation of ultraviolet (UV) light, which accounts for merely 5% of sunlight, and therefore their practical applications are limited. The development of visible light-driven photocatalysts and photo-Fenton-like catalysts is necessary for their applications in the wastewater treatment.

$BiFeO_3$ is one of the important perovskite-type oxides with a narrow band gap of 2.1–2.5 eV, which is suitable for the response of visible light. $BiFeO_3$ is shown to be a promising photocatalyst for dye degradation, as well as water splitting under visible-light irradiation [20–27]. Furthermore, $BiFeO_3$ also exhibits favorable visible-light-driven photo-Fenton degradation activity [28,29]. Unfortunately, $BiFeO_3$ still exhibits a high recombination rate of photoproduced electron-hole pairs, and thus its photocatalytic and photo-Fenton catalytic activity is limited. Until now, many strategies have been developed to enhance the separation rate of photogenerated charges, such as doping with other elements, decoration with noble metals, and construction of heterojunction composites [30–34]. Especially, coupling $BiFeO_3$ with an appropriate semiconductor to form the Z-scheme heterojunction was reported to be an efficient and promising strategy, to suppress the recombination of photogenerated charges, and then to enhance its catalytic activity [35–37].

Low-dimension nanomaterials like graphene, carbon nanotubes, carbon quantum dots (CQDs), SiC nanowires, and $Ag_2S$ nanoparticles manifest many attractive properties, and they offer great potential applications for bioimaging, energy conversion, optoelectronic devices, wave absorption, and sensors [38–51]. Moreover, these nanomaterials have been widely used as modifiers or cocatalysts to improve the photocatalytic performances of semiconductors [52–56]. Among them, $Ag_2S$ is a narrow band-gap semiconductor, and they can absorb visible and near-infrared light. This makes it an important visible-light-driven photocatalytic material [57,58]. Particularly, $Ag_2S$ has been most frequently used as an ideal co-catalyst, combined with other semiconductors, to form heterojunction composites with improved catalytic activity [59–62]. Moreover, the construction of heterostructures can significantly decrease the photocorrosion of $Ag_2S$. It is noted that bare $Ag_2S$ could easily undergo photocorrosion, due to the reduction of the lattice $Ag^+$ into metal Ag, caused by photogenerated electrons. By comparing the energy band position and bandgap of $Ag_2S$ with those of $BiFeO_3$, the two semiconductors are expected to be coupled together to form excellent Z-scheme $Ag_2S/BiFeO_3$ heterojunction composites. However, no work has been found that is concerned with the visible-light-driven photocatalytic and photo-Fenton catalytic activities of Z-scheme $Ag_2S/BiFeO_3$ composites.

In this work, $Ag_2S$ nanoparticles were decorated on the surfaces of polyhedral $BiFeO_3$ particles to produce Z-scheme $Ag_2S/BiFeO_3$ heterojunction composites via a co-precipitation method. The photocatalytic and photo-Fenton catalytic degradation activities of the $Ag_2S/BiFeO_3$ composites was systematically investigated by degrading methyl orange (MO), using visible light as the light source. The underlying catalytic mechanism of the composites was proposed.

## 2. Theoretical Methods

### 2.1. Preparation of the $Ag_2S$ Nanoparticles

For the preparation of $Ag_2S$, 2 mmol of $AgNO_3$ was introduced into 30 mL deionized water, and magnetically stirred to obtain a uniform solution. Exactly 1 mmol of $Na_2S$ was dissolved in 20 mL

deionized water, and the resulting $Na_2S$ solution was then added into the $AgNO_3$ solution (above). The mixture was subjected to vigorous magnetic stirring for 5 h. During this process, a black suspension was obtained. The black product was collected by centrifugation. After washing several times using deionized water and then drying at 60 °C for 6 h in a vacuum oven, the final $Ag_2S$ nanoparticles were obtained.

## 2.2. Preparation of BiFeO₃ Polyhedra

For the synthesis of $BiFeO_3$, 5 mmol of $Bi(NO_3)_3 \cdot 5H_2O$ and 5 mmol of $Fe(NO_3)_3 \cdot 9H_2O$ were added into 20 mL of 25% (*v/v*) dilute nitric acid solution under magnetic stirring. Exactly 60 mL of $4.5 \text{ mol} \cdot L^{-1}$ KOH solution was dropped into the above solution. After magnetic stirring and ultrasonic treatment, a yellow suspension was obtained. Then, the suspension was transferred into a Teflon-lined stainless steel autoclave (capacity: 100 mL), and heated at 200 °C for 9 h. After that, the product was collected and washed with deionized water. After drying at 80 °C for 12 h, the final product of the $BiFeO_3$ polyhedra was obtained.

## 2.3. Fabrication of the Ag₂S/BiFeO₃ Composites

For the fabrication of the $Ag_2S/BiFeO_3$ composites, 0.1 g of $BiFeO_3$ particles and a certain amount of $AgNO_3$ were added into 30 mL of deionized water under vigorous stirring, to achieve a uniform mixture. Exactly 20 mL $Na_2S$ solution (possessing a certain concentration) was slowly added into the above suspension, which was then subjected to magnetic stirring for 5 h. In this process, the color of the mixture changed from brownish into black, indicative of the successful assembly of $Ag_2S$ nanoparticles on the surface of the $BiFeO_3$ polyhedral particles. After washing and drying, as in the procedure described above, the final $Ag_2S/BiFeO_3$ composite was obtained. By adjusting the amounts of $AgNO_3$ and $Na_2S$, a series of $Ag_2S/BiFeO_3$ composites with different $Ag_2S$ mass fractions (5%, 10%, 15%, and 20%) in the composites were fabricated. The corresponding composites were named 5% $Ag_2S/BiFeO_3$, 10% $Ag_2S/BiFeO_3$, 15% $Ag_2S/BiFeO_3$, and 20% $Ag_2S/BiFeO_3$.

## 2.4. The Photo-Fenton Catalytic Activity Test

To investigate the photo-Fenton catalytic activities of the samples, MO was used as the model pollutant, and the visible light (300 W xenon lamp with a 420 nm cut-off filter) was used as the light source. A certain amount of the catalyst was dispersed into the MO solution (100 mL) in the dark under magnetic stirring for 30 min. During this process, the absorption/desorption equilibrium between the catalyst and the dye was achieved. After that, an amount of $H_2O_2$ was added into the reaction solution, and then irradiated by visible light. During the reaction, 2.5 mL of the reaction solution was sampled at a given time interval, and centrifuged to remove the catalyst. The residual MO concentration was obtained by measuring the absorbance of the reaction solution at $\lambda_{MO}$ = 464 nm. The effects of catalyst dosage, $H_2O_2$ concentration, and MO concentration on the degradation efficiency of MO were investigated, based on the above experimental process. The photocatalytic activity of the samples was evaluated under the same conditions without the addition of $H_2O_2$. Ethanol (10% (*v/v*)), ammonium oxalate (AO, $2 \text{ mmol} \cdot L^{-1}$) and benzoquinone (BQ, $1 \text{ mmol} \cdot L^{-1}$) were separately added into the reaction solution, with the aim of examining the active species in the catalytic process.

## 2.5. Photoelectrochemical Measurement

An electrochemical workstation (CHI 660C, Shanghai Chenhua Instrument Co. Ltd, Shanghai, China) with a three-electrode system was used for the photoelectrochemical measurements [63]. In the three-electrode system, a platinum foil acted as the counter-electrode, and a standard calomel electrode was used as the reference electrode. For the preparation of the working electrode, stoichiometric amounts of photocatalyst (15 mg), carbon-black (0.75 mg), and polyvinylidene fluoride (PVDF, 0.75 mg) were uniformly dispersed in 1 mL 1-methyl-2-pyrrolidone (NMP) to obtain a slurry mixture. The slurry mixture was coated onto a fluoride-doped tin oxide glass electrode (effective area: $1.0 \times 1.0 \text{ cm}^2$), and

dried at 60 °C for 5 h. During the photoelectrochemical measurements, a 300 W xenon lamp with a 420 nm cut-off filter was used as the light source, and 1 mol $L^{-1}$ $Na_2SO_4$ aqueous solution was used as the electrolyte. A 0.2 V bias potential was applied for the testing of photocurrent–time (*I-t*) curves. The electrochemical impedance spectroscopy (EIS) spectra were recorded by applying a sinusoidal voltage pulse (amplitude: 5 mV; frequency range: $10^{-2}$–$10^5$ Hz).

*2.6. Hydroxyl Radical Measurement*

The •OH radicals generated on the irradiated samples were measured by fluorimetry. To achieve this aim, terephthalic acid (TA) as an •OH scavenger [64]. The measurement procedure was as follows: TA was added into an NaOH solution with a concentration of 1.0 mmol·$L^{-1}$, to obtain a 0.25 mmol·$L^{-1}$ TA solution. Exactly 60 mg of the catalyst was added into 100 mL of TA solution. The mixture was magnetically stirred for several minutes to ensure the uniform dispersion of the catalyst. Subsequently, $H_2O_2$ was added into the reaction solution (2.0 mmol·$L^{-1}$) and then irradiated by a 300 W xenon lamp with a 420 nm cut-off filter. At a given time interval, 2.5 mL of the reaction solution was sampled to measure its photoluminescence (PL) spectrum (the catalyst was removed by centrifugation). A fluorescence spectrophotometer was used to measure the PL spectrum of the reaction solution (excitation wavelength: 315 nm). The •OH radicals produced during the photocatalytic process were detected under the same conditions without the introduction of $H_2O_2$.

*2.7. Characterization*

X-ray powder diffraction (XRD) was employed to investigate the phase purity of the samples on a D8 Advance X-ray diffractometer (Bruker AXS, Karlsruhe, Germany). The morphologies and microstructures of the products were observed by field-emission scanning electron microscopy (SEM) and field-emission transmission electron microscopy (TEM). The SEM investigation was performed on a JSM-6701F scanning electron microscope (JEOL Ltd., Tokyo, Japan), and the TEM observation was carried out on a JEM-1200EX transmission electron microscope (JEOL Ltd., Tokyo, Japan). X-ray photoelectron spectroscopy (XPS) was used to record the chemical states of the elements on a PHI-5702 multi-functional X-ray photoelectron spectrometer (Physical Electronics, Chanhassen, MN, USA). The ultraviolet–visible (UV-Vis) diffuse reflectance spectra of the samples were tested by using a TU-1901 double beam UV-Vis spectrophotometer (Beijing Purkinje General Instrument Co. Ltd., Beijing, China) with $BaSO_4$ as a reference. An RF-6000 fluorescence spectrophotometer (Shimadzu, Kyoto, Japan) was available to record the PL spectra of the samples (excitation wavelength: ~350 nm).

## 3. Results and Discussion

*3.1. XRD Analysis*

Figure 1 shows the XRD patterns of the $BiFeO_3$, $Ag_2S$ and $Ag_2S/BiFeO_3$ composites. For the bare $BiFeO_3$ and $Ag_2S$ samples, their diffraction peaks could be completely indexed in terms of the rhombohedral structure of $BiFeO_3$ (PDF card no. 74-2016) and the monoclinic structure of $Ag_2S$ (PDF card no. 14-0072), respectively. When $Ag_2S$ is decorated on $BiFeO_3$, the diffraction peaks of $BiFeO_3$ undergo no obvious change, suggesting that $BiFeO_3$ maintains a rhombohedral structure. Meanwhile, weak characteristic diffraction peaks of $Ag_2S$ are observed in the composites, indicating the decoration of $Ag_2S$ on $BiFeO_3$. In addition, no other impurity phases are detected in the composites.
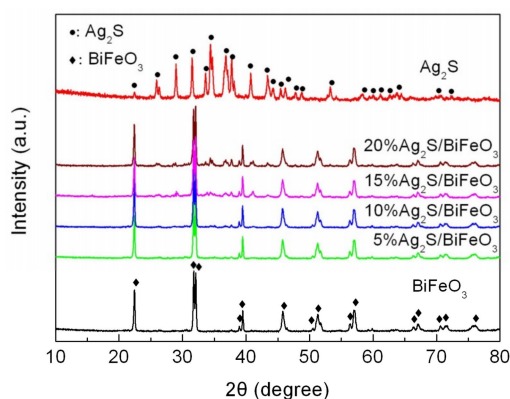
**Figure 1.** X-ray powder diffraction (XRD) patterns of $BiFeO_3$, $Ag_2S$, and $Ag_2S/BiFeO_3$ composites.

## 3.2. Optical Absorption Properties

Figure 2a shows the absorption spectra of the $BiFeO_3$ and $Ag_2S/BiFeO_3$ composites transformed from the UV-Vis spectra, using the Kubelka–Munk (K-M) theory. It is worth noting that, with the increase of $Ag_2S$ content, the composites exhibit a gradually increasing light absorption over the whole wavelength range, which is mainly due to the strong light absorption of $Ag_2S$ in the UV-Vis light region. The digital images of the samples inserted in Figure 2a show that the color of bare $BiFeO_3$ is brown, and the 15% $Ag_2S/BiFeO_3$ composite manifests a black color. The deepening of the apparent color for the composite further confirms its enhanced visible-light absorption. To obtain the energy bandgap of the samples, the plots of $(\alpha h\nu)^2$ vs $h\nu$ using the Tauc relation are carried out, where $\alpha$ is defined as the K-M absorption coefficient, and $h\nu$ is the incident photon energy. As depicted in Figure 2b, the bandgap ($E_g$) of bare $BiFeO_3$ is estimated to be 2.15 eV by extrapolating the linear portion of the plot to the $h\nu$ axis. A similar $E_g$ of $BiFeO_3$ in the 20% $Ag_2S/BiFeO_3$ composite is obtained, suggesting that the band structure of $BiFeO_3$ undergoes no detectable change after the decoration of $Ag_2S$. In addition, based on its bandgap energy, the valence band (VB) and the conduction band (CB) potentials of $BiFeO_3$ can be obtained by using the following relations (Equations (1) and (2)):

$$E_{VB} = X - E^e + 0.5\,E_g \tag{1}$$
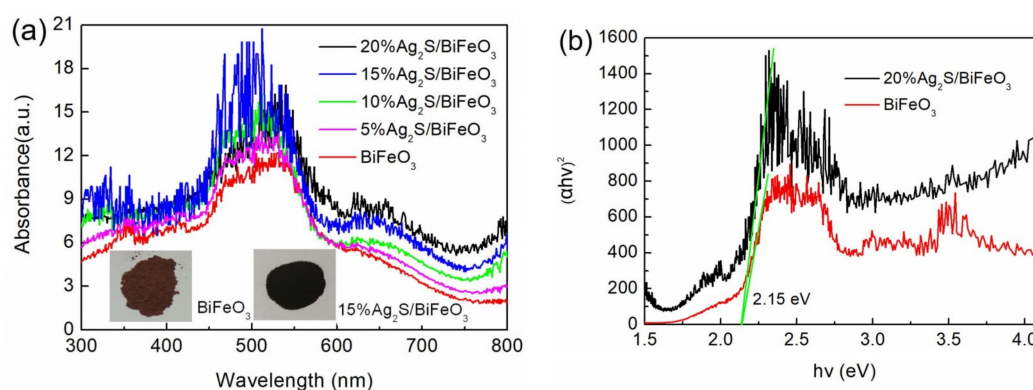
$$E_{CB} = X - E^e - 0.5\,E_g \tag{2}$$



**Figure 2.** (**a**) UV-Vis absorption spectra of $BiFeO_3$ and $Ag_2S/BiFeO_3$ composites. The insets show the digital images of $BiFeO_3$ and 15% $Ag_2S/BiFeO_3$. (**b**) The corresponding Tauc plots of $(\alpha h\nu)^2$ vs $h\nu$ for $BiFeO_3$ and 20% $Ag_2S/BiFeO_3$.

In the above relations, $X$ is the absolute electronegativity of $BiFeO_3$, and it is estimated to be 5.93 eV, based on the data reported in the literature [65]. $E^e$ is defined as the energy of free electrons on the hydrogen scale (~4.5 eV). The VB and CB potentials of $BiFeO_3$ were found to be +2.5 and +0.35 V vs normal hydrogen electrode (NHE), respectively.

### 3.3. XPS Analysis

To investigate the surface chemical states of 15% $Ag_2S/BiFeO_3$, XPS detection was carried out. Figure 3a–e show the high-resolution XPS spectra of Bi 4f, Fe 2p, O 1s, Ag 3d, and S 2p, respectively. From Figure 3a, the Bi $4f_{5/2}$ and Bi $4f_{7/2}$ binding energy peaks were found at 163.9 and 158.7 eV, respectively, indicating the existence of $Bi^{3+}$ [21]. Figure 3b depicts the Fe 2p spectrum, which displays two separate peaks at 724.2 (Fe $2p_{1/2}$) and 710.1 eV (Fe $2p_{3/2}$), respectively. The Fe $2p_{3/2}$ binding energy can be divided into two peaks at 711.3 and 709.8 eV, corresponding to $Fe^{3+}$ and $Fe^{2+}$, respectively [21,66,67]. The weak peak detected at 718.6 eV is characterized as the satellite peak for $Fe^{3+}$. Figure 3c presents the O 1s spectrum. By fitting the O 1s binding energy, two peaks at 529.3 and 531.1 eV are found. The signal at 529.3 eV is assigned to the lattice oxygen, while the peak at 531.1 eV is mainly attributed to the surface vacancies and the chemisorbed oxygen [21,62]. On the Ag 3d spectrum (Figure 3d), the peak at 368.4 eV is assigned to Ag $3d_{5/2}$, and the peak at 374.3 eV is attributed to Ag $3d_{3/2}$ of $Ag^+$ [68]. In the spectrum of S 2p (Figure 3e), the signal of S 2p can be deconvoluted into two peaks at 162.7 and 161.5 eV, which are caused by the S $2p_{1/2}$ and S $2p_{3/2}$, respectively [68].
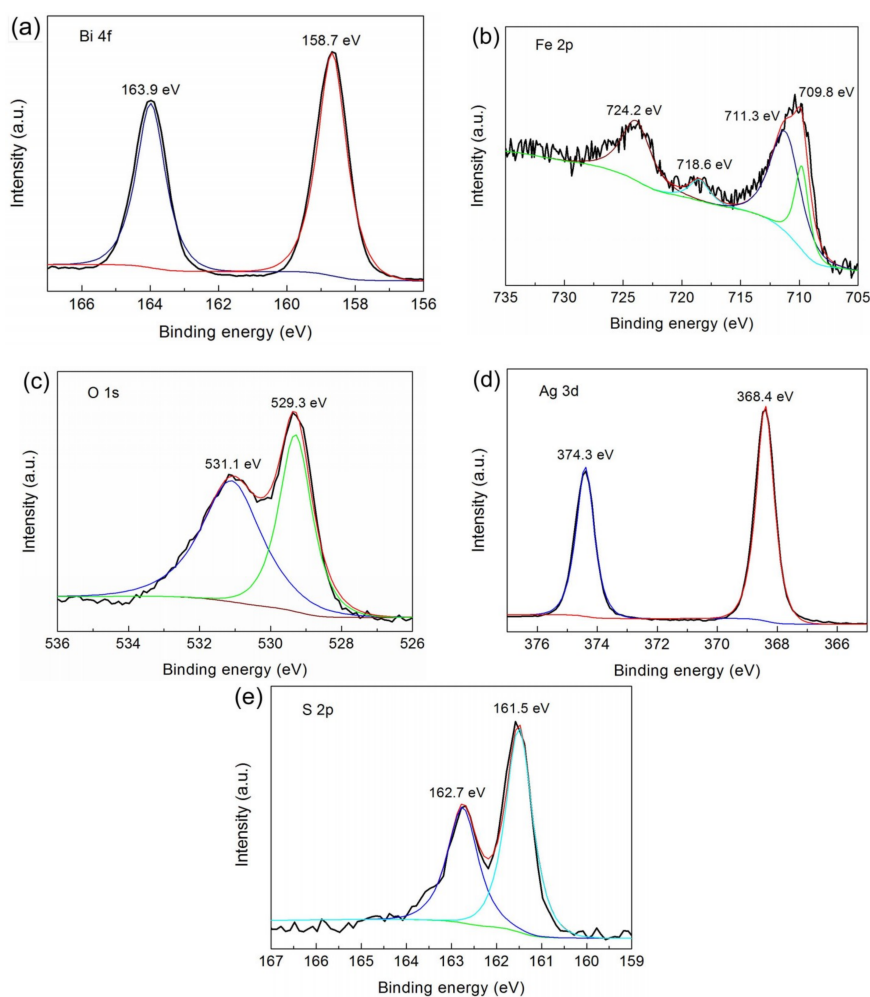


**Figure 3.** High-resolution X-ray photoelectron spectroscopy (XPS) spectra of the 15% $Ag_2S/BiFeO_3$ composite. (**a**) Bi 4f; (**b**) Fe 2p; (**c**) O 1s; (**d**) Ag 3d; (**e**) S 2p.

### 3.4. Morphology Observations

Figure 4a–d shows the SEM images of $Ag_2S$, $BiFeO_3$, and 15% $Ag_2S/BiFeO_3$. It is seen that $Ag_2S$ exhibits spherical-like shapes with diameters of 30–50 nm. The $BiFeO_3$ sample is mainly composed of polyhedral-like particles with edge lengths of 500–800 nm, and the particles have smooth surfaces. From the SEM image of the 15% $Ag_2S/BiFeO_3$ composite, small $Ag_2S$ nanoparticles are clearly observed to be attached onto the surface of the $BiFeO_3$ polyhedral-like particles. Figure 4e presents the TEM image of the 15% $Ag_2S/BiFeO_3$ composite, further confirming the decoration of the $Ag_2S$ nanoparticles on the polyhedral $BiFeO_3$ particles. The high-resolution TEM (HRTEM) image obtained from the interface of the two phases in the 15% $Ag_2S/BiFeO_3$ composite is shown in Figure 4f, revealing two distinct sets of lattice fringes. The interplanar spacing of ~0.39 nm corresponds to the (012) plane of $BiFeO_3$, and the interplanar spacing of ~0.27 nm corresponds to the (122) plane of $Ag_2S$. This indicates the intimate contact between $Ag_2S$ and $BiFeO_3$ to form a $Ag_2S/BiFeO_3$ heterojunction structure. To further investigate the distribution of $Ag_2S$ on the surface of $BiFeO_3$, the elemental mapping observation of 15% $Ag_2S/BiFeO_3$ was performed, as shown in Figure 5. Figure 5a depicts the dark-field scanning TEM (DF-STEM) image of the composite, and Figure 5b–f display the corresponding elemental maps that are obtained according to the procedure described in the literature [69]. It was found that large-sized polyhedra show an elemental distribution of Bi, Fe and O, whereas the attached small particles contain the elements Ag and S. The result suggests that the $Ag_2S$ nanoparticles are uniformly anchored onto the surface of the polyhedral $BiFeO_3$ particles.
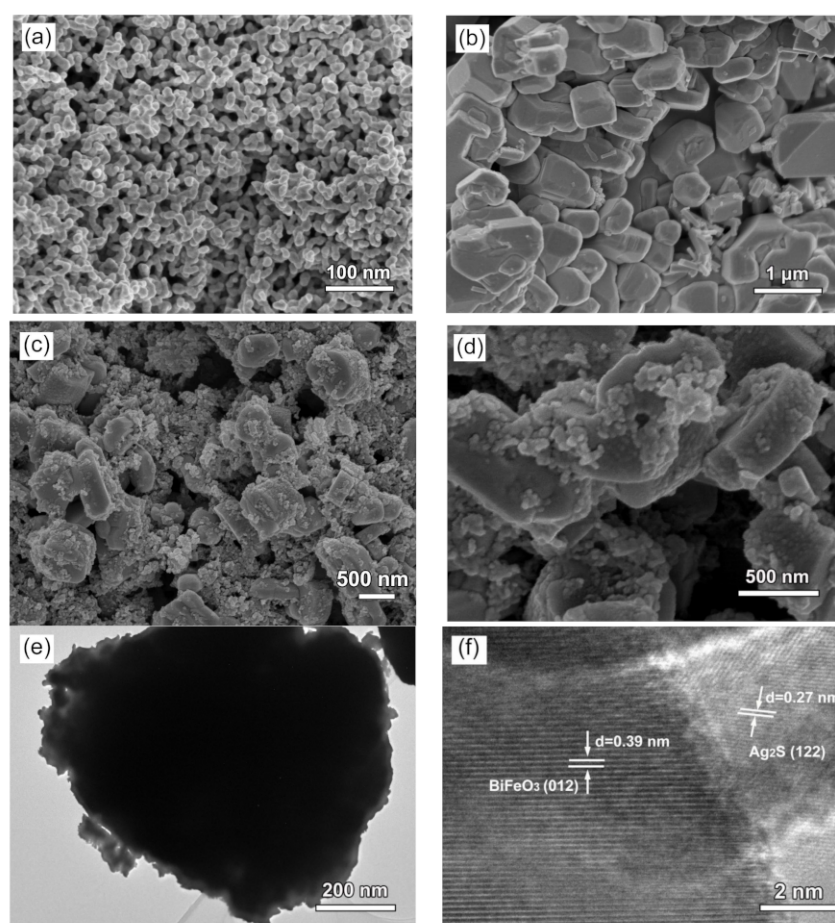


**Figure 4.** (**a**–**d**) Scanning electron microscopy (SEM) images of $Ag_2S$ nanoparticles, $BiFeO_3$ particles and 15% $Ag_2S/BiFeO_3$, respectively. (**e**) and (**f**) Transmission electron microscopy (TEM) image and high-resolution (HR)TEM image of 15% $Ag_2S/BiFeO_3$, respectively.

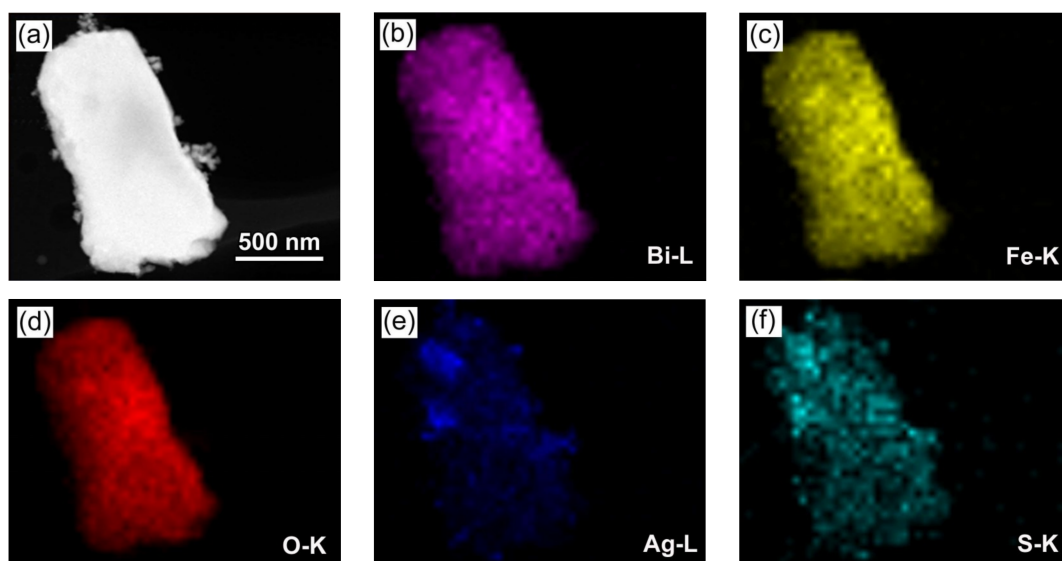**Figure 5.** (**a**) Dark-field scanning TEM (DF-STEM) image of 15% Ag$_2$S/BiFeO$_3$. (**b**–**f**) The energy-dispersive X-ray elemental mapping images of the region shown in (a).

## *3.5. Photo-Fenton Catalytic and Photocatalytic Performances*

MO was used as the model pollutant to evaluate the visible-light-driven photocatalytic activities of the samples, as shown in Figure 6a. The direct photolysis of the dye without the photocatalyst, and the dye adsorption on the photocatalyst were also investigated, which reveals that the dye MO has a good stability after a short period of visible-light irradiation; the absorption of the dye on the photocatalyst is very small. After 4 h of photocatalysis, the introduction of BiFeO$_3$ and Ag$_2$S leads to MO degradation percentages of ~33% and ~30%, respectively. This implies a relatively weak photocatalytic activity from bare BiFeO$_3$ and Ag$_2$S. When Ag$_2$S is decorated on BiFeO$_3$, the formed Ag$_2$S/BiFeO$_3$ composites exhibit obviously improved photocatalytic activities. With an increase in the Ag$_2$S content, an optimal composite sample is observed for 15% Ag$_2$S/BiFeO$_3$. Further increasing the Ag$_2$S content cannot result in an enhanced photocatalytic activity for the composites. This suggests that the construction of the Ag$_2$S/BiFeO$_3$ heterojunction is critical for the effective enhancement of photocatalytic activity. However, the excessive Ag$_2$S loading may result in full coverage by Ag$_2$S on the BiFeO$_3$ surface, thus decreasing the photon absorption of BiFeO$_3$. To further compare the photocatalytic activities of the samples, kinetic analysis of the photocatalytic degradation of MO was carried out. As illustrated in Figure 6c, the plots of Ln($C_t$/$C_0$) vs reaction time $t$ presented a good linear behavior, and they can be modeled well by using the first-order kinetic equation Ln($C_t$/$C_0$) = $k_{app}t$, where $k_{app}$ is the apparent first-order reaction rate constant. In every case, the standard deviation (SD) was smaller than 0.07. The obtained values of $k_{app}$ and SD are inserted in Figure 6c. From the reaction rate constants, it is concluded that the optimal composite sample, 15% Ag$_2$S/BiFeO$_3$, has a photocatalytic activity ca. 4.0 and 4.1 times higher than those of bare BiFeO$_3$ and Ag$_2$S, respectively.

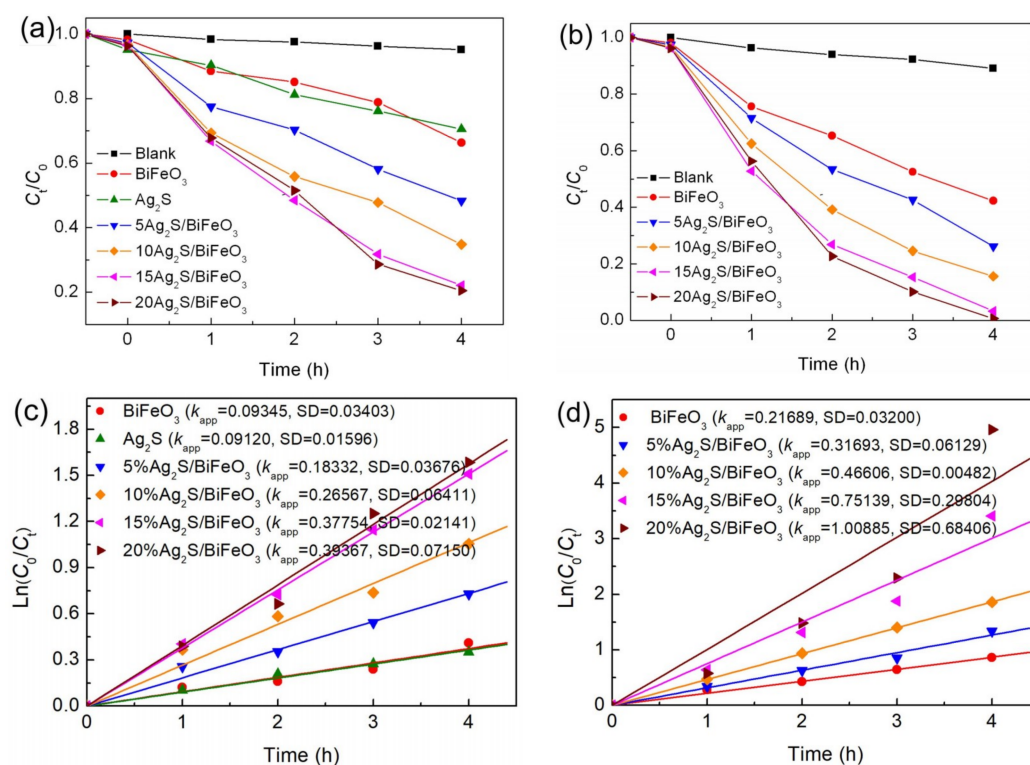**Figure 6.** (**a**) Photocatalytic activities of $Ag_2S$, $BiFeO_3$, and $Ag_2S/BiFeO_3$ composites toward the degradation of MO under visible-light irradiation, along with the blank and adsorption experiment results. (**b**) Photo-Fenton catalytic activities of $BiFeO_3$ and $Ag_2S/BiFeO_3$ composites toward the degradation of MO under visible-light irradiation, and in the presence of $H_2O_2$, along with blank and adsorption experimental results. (**c**) Plots of $Ln(C_t/C_0)$ vs reaction time $t$ for the photocatalytic degradation of MO over the samples. (**d**) Plots of $Ln(C_t/C_0)$ vs reaction time $t$ for the photo-Fenton catalytic degradation of MO over the samples.

To further examine the photo-Fenton catalytic behavior of the samples, the degradation of MO in the photo-Fenton processes was performed, as shown in Figure 6b. In the absence of the photocatalyst, the degradation of MO is observed to be very small under visible light irradiation and in the presence of $H_2O_2$, indicating minor self-degradation for MO. With the addition of catalysts and $H_2O_2$ under visible light irradiation, dye degradation is significantly enhanced, to be much higher than that in the bare photocatalytic process. The photo-Fenton catalytic activities of the samples are in the same orders as their photocatalytic activities. The kinetic plots for the photo-Fenton catalytic degradation of MO are shown in Figure 6d. The derived reaction rate constants reveal that the 15% $Ag_2S/BiFeO_3$ composite exhibits a photo-Fenton catalytic activity ca. 3.5 times higher than that of bare $BiFeO_3$.

Figure 7 shows the degradation percentage of MO over the 15% $Ag_2S/BiFeO_3$ composite during three successive photocatalytic or photo-Fenton catalytic processes. It is seen that the catalytic activity of the composite does not undergo a significant decrease. After three successive recycles, the photocatalytic and photo-Fenton catalytic degradation percentages of MO still reach ~70% and ~84%, respectively.
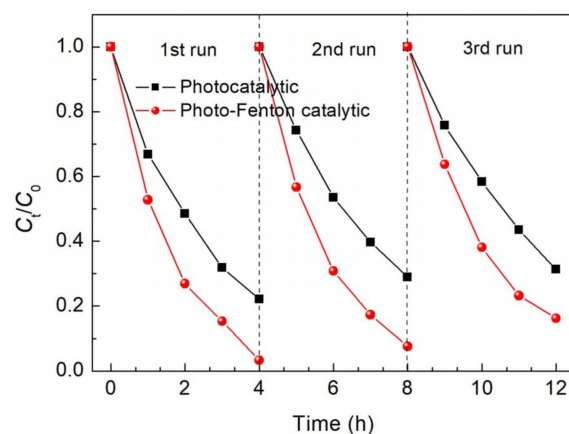
**Figure 7.** Photocatalytic and photo-Fenton catalytic recyclabilities of the 15% Ag$_2$S/BiFeO$_3$ composite for the degradation of MO under visible-light irradiation.

Choosing 15% Ag$_2$S/BiFeO$_3$ as the photocatalyst, further photo-Fenton degradation experiments were carried out, aimed at investigating the effects of photocatalyst dosage, H$_2$O$_2$ content, and dye concentration on dye degradation. Figure 8a shows the effect of catalyst dosage on the degradation of MO. The corresponding kinetic plots are presented in Figure 8b. The degradation percentage of MO increases gradually with an increase in the catalyst loading from 0.1 to 0.6 g·L$^{-1}$. However, when the catalyst loading exceeds the optical value (0.6 g·L$^{-1}$), the catalytic efficiency starts to decrease. Generally, increasing the catalyst loading can provide more active sites for H$_2$O$_2$ activation to produce more •OH radicals, thus accelerating the degradation of the dye. Nevertheless, excessive addition of the catalyst will enhance the light screening effect, and reduce light absorption, thus resulting in a decrease in the catalytic efficiency.
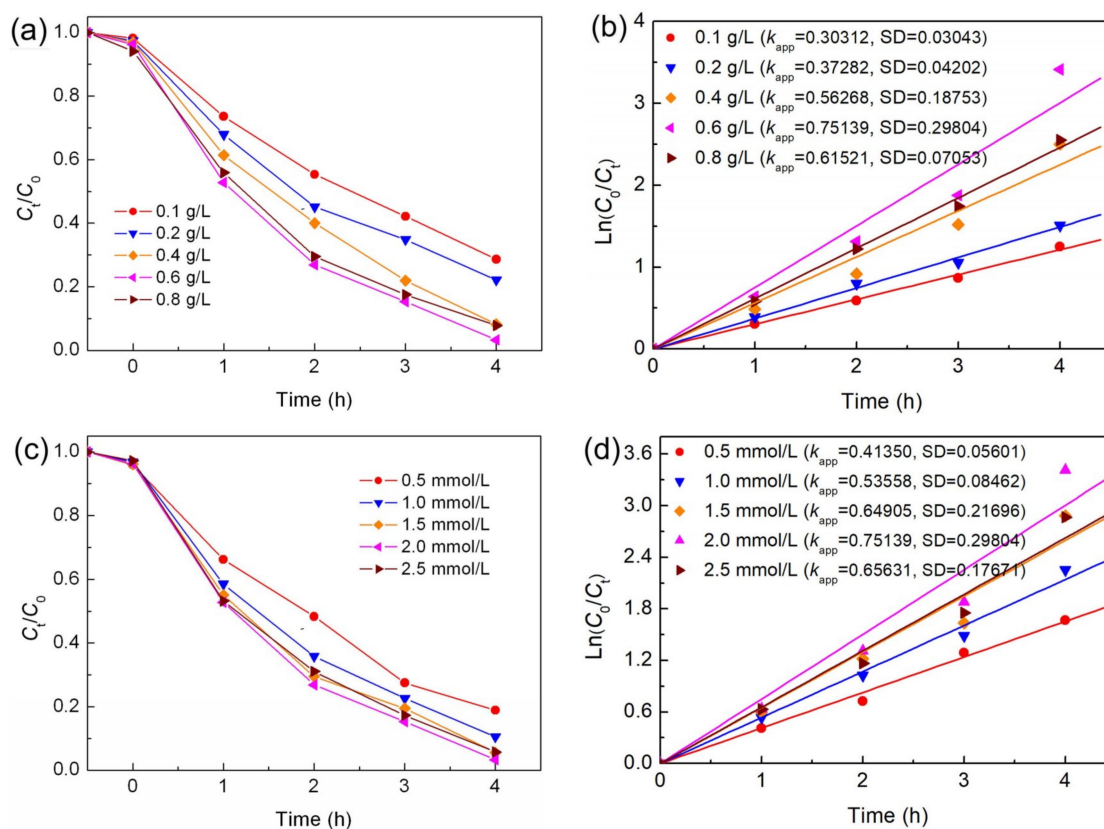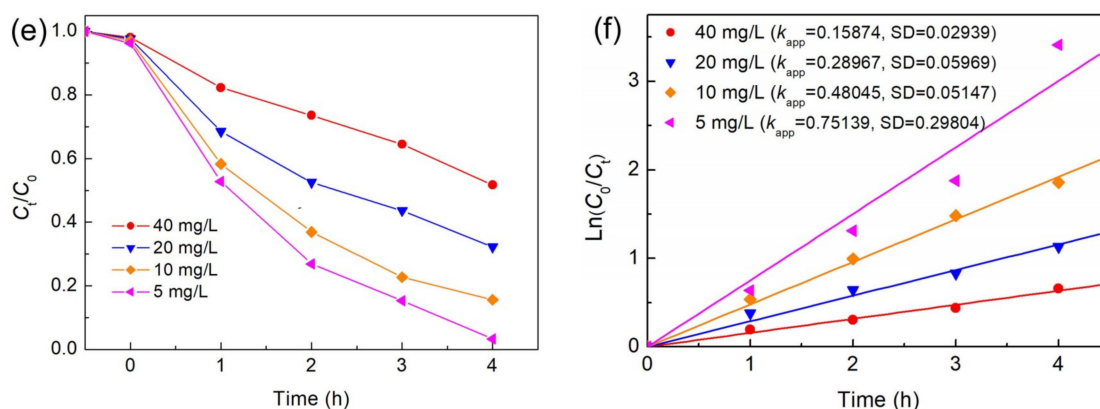


**Figure 8.** *Cont.*

**Figure 8.** Effects of the photocatalyst (15% $Ag_2S/BiFeO_3$) dosage (**a**) and (**b**), $H_2O_2$ content (**c**) and (**d**), and MO concentration (**e**) and (**f**) on the photo-Fenton catalytic degradation of MO, respectively.

The effect of $H_2O_2$ concentration on the degradation of MO is shown in Figure 8c. As observed, the degradation percentage of MO increases from ~81% to ~97%, with an increase in the $H_2O_2$ concentration from 0.5 to 2 mmol·$L^{-1}$, which is due to the fact that more •OH radicals can be produced by increasing the $H_2O_2$ concentration. However, when the concentration of $H_2O_2$ reaches 2.5 mmol·$L^{-1}$, the MO degradation percentage exhibits a decreasing trend. This phenomenon is mainly attributed to the consumption of •OH radicals by the reaction of additional $H_2O_2$ with •OH [15]. The corresponding kinetic plots and derived reaction rate constants (Figure 8d) further confirm the effect of $H_2O_2$ concentration on the degradation of MO.

The effect of MO concentration on its degradation is shown in Figure 8e. The corresponding kinetic plots are presented in Figure 8f. It is seen that the degradation percentage of MO decreases with increasing the initial MO concentration, which is due to the decreased light transparency. In spite of this, the 15% $Ag_2S/BiFeO_3$ composite still photo-Fenton-catalyzes a 50% rate of removal of the dye at a high MO concentration of 40 mg·$L^{-1}$. This implies that the present $Ag_2S/BiFeO_3$ composite photocatalyst could offer a practical application in the treatment of high-concentration dye wastewater. From an application viewpoint, the stability of the catalyst is another important factor to be considered besides its catalytic activity.

### 3.6. Photogenerated Charge Behavior

It is known that photocatalytic and photo-Fenton catalytic activities are related to the performance of the photogenerated charges. Photoelectrochemical and PL measurements were performed to investigate the photoinduced charge behaviors of the samples [70,71]. Figure 9a shows the photocurrent response profiles of $BiFeO_3$ and 15% $Ag_2S/BiFeO_3$. Compared with bare $BiFeO_3$, the 15% $Ag_2S/BiFeO_3$ composite exhibits an enhanced photocurrent density, suggesting that the decoration of $Ag_2S$ nanoparticles results in an enhanced separation of photogenerated $e^-$-$h^+$ pairs. The EIS spectra of $BiFeO_3$ and 15% $Ag_2S/BiFeO_3$ are presented in Figure 9b. In the EIS spectra, the arc radius for 15% $Ag_2S/BiFeO_3$ is smaller than that for bare $BiFeO_3$, which indicates the low interfacial resistance of the composite. Figure 9c displays the PL spectra of $BiFeO_3$ and 15% $Ag_2S/BiFeO_3$. A steady emission peak is detected at ~520 nm, which is mainly due to the recombination of the photogenerated charges. The 15% $Ag_2S/BiFeO_3$ composite possesses a relatively weak PL emission peak in comparison to bare $BiFeO_3$, indicating that the recombination of photoinduced charges is suppressed in the composite. The above results reveal that the photogenerated electrons and holes of $BiFeO_3$ are successfully separated and migrated by the decorations of the $Ag_2S$ nanoparticles.
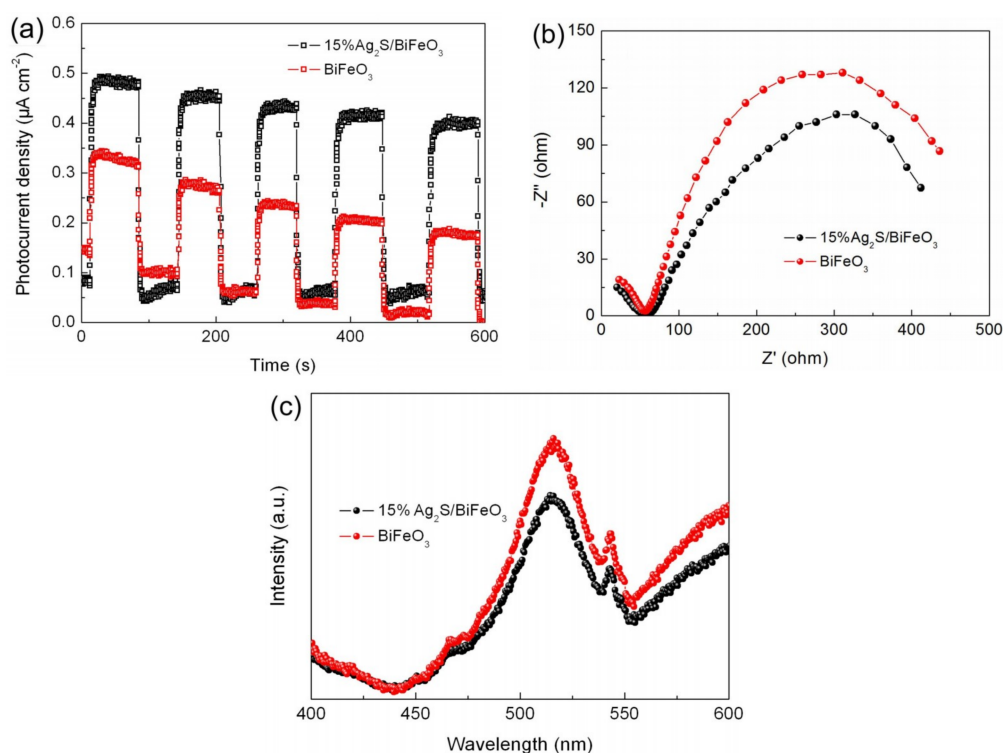
**Figure 9.** Transient photocurrent response curves under intermittent irradiation with visible light (**a**), Nyquist plots of the electrochemical impedance spectroscopy (EIS) spectra under visible-light irradiation (**b**), and PL spectra (**c**) of $BiFeO_3$, and 15% $Ag_2S/BiFeO_3$.

### 3.7. Active Species Detection

To unveil the active species that are responsible for the photocatalytic and photo-Fenton catalytic degradation of MO over the $Ag_2S/BiFeO_3$ composites, the active species trapping experiments were performed. To achieve this aim, ethanol was used as the •OH scavenger, AO as the $h^+$ scavenger, and BQ as the $•O_2^-$ scavenger [72], and the results are shown in Figure 10. During the photocatalytic process, the introduction of AO leads to an obvious reduction of dye degradation, and a similar suppression effect is detected after the addition of BQ. When ethanol is added, the degradation efficiency of the dye is slightly decreased. The above results suggest that $h^+$ and $•O_2^-$ are considered to be the major reactive species, while •OH plays a relatively small role in the photocatalytic degradation of MO. In the photo-Fenton catalytic reaction, ethanol can greatly inhibit the degradation of MO. Compared with ethanol, AO and BQ exhibit relatively weak inhibition effects on dye degradation. This indicates that the photo-Fenton catalytic degradation of MO over the $Ag_2S/BiFeO_3$ composite is primarily induced by the attack of $h^+$, $•O_2^-$, and •OH, and •OH plays a relatively large role in the photo-Fenton catalytic reaction.
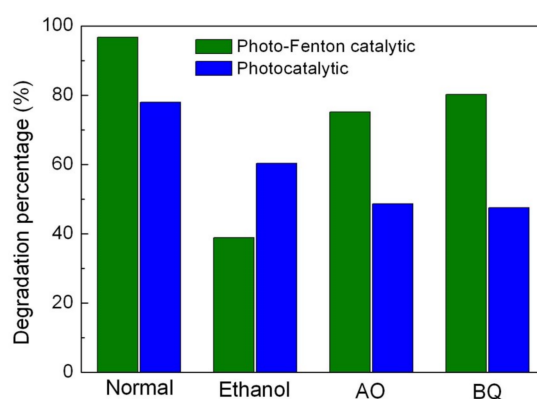
**Figure 10.** Effects of ethanol, benzoquinone (BQ) and ammonium oxalate (AO) on the photocatalytic and photo-Fenton catalytic degradation rates of MO over 15% $Ag_2S/BiFeO_3$ under visible-light irradiation.

Figure 11a,b shows the time-dependent PL spectra of the TPA solution over the 15% $Ag_2S/BiFeO_3$ composite in the photocatalytic and the photo-Fenton catalytic processes, respectively. During the photocatalytic and photo-Fenton catalytic processes, an obvious PL signal is detected at around 429 nm, and its intensity exhibits an increasing trend with the irradiation time, suggesting that the production of the •OH radicals during the photocatalytic and photo-Fenton catalytic processes. However, the PL signal becomes more intense in the photo-Fenton process, which indicates the generation of more •OH radicals. This result is consistent with the active species-trapping experiments.



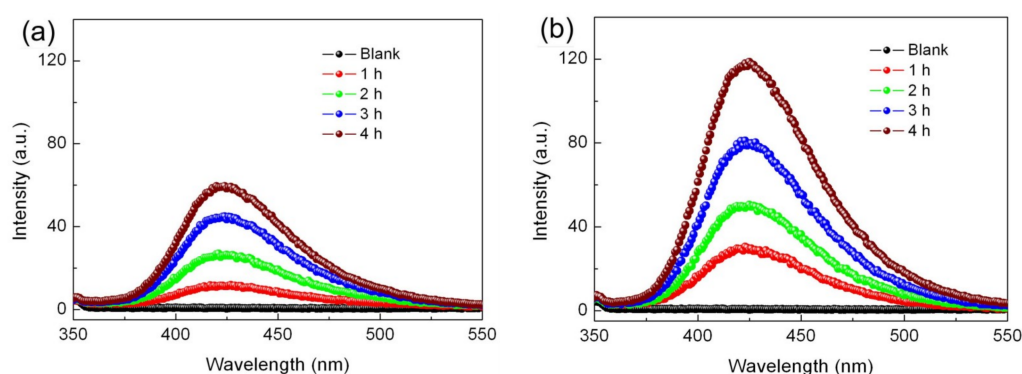**Figure 11.** Time-dependent PL spectra of the terephthalic acid (TA) solution after (**a**) photocatalytic and (**b**) photo-Fenton reactions over 15% $Ag_2S/BiFeO_3$.

*3.8. Photocatalytic and Photo-Fenton Mechanisms*

The photocatalytic mechanism of the $Ag_2S/BiFeO_3$ composites are schematically shown in Figure 12a. Based on the previous report, the CB/VB edge potentials of $Ag_2S$ are estimated to be $-0.3/+0.7$ V vs NHE [73]. The CB/VB edge potentials of $BiFeO_3$ are obtained as $+0.35/+2.5$ V vs NHE, respectively. This suggests that $BiFeO_3$ and $Ag_2S$ can be coupled together to form a promising Z-scheme composite photocatalysts, due to their well-matched overlapping band-structures. Under illumination from visible light, both $BiFeO_3$ and $Ag_2S$ are excited to generate electrons in the CB, and holes in the VB. For bare $BiFeO_3$ and $Ag_2S$, most of the photogenerated charges tend to be recombined, and only a few of them take part in the photocatalytic reaction. In contrast, in the $Ag_2S/BiFeO_3$ heterojunction composites, the photoexcited electrons in the CB of $BiFeO_3$ will migrate to $Ag_2S$ and combine with the photoexcited holes in the VB of $Ag_2S$. This charge migration and combination process remarkably promote the separation of the photogenerated electrons, and holes in $BiFeO_3$ and $Ag_2S$. As a result, more photoinduced holes in $BiFeO_3$ and photoinduced electrons in $Ag_2S$ are able to take part

in the photocatalytic reaction. This is the dominant mechanism, resulting in enhanced photocatalytic activity for the $Ag_2S/BiFeO_3$ composites. Compared to the redox potential of $O_2/\bullet O_2^-$ ($-0.13$ V vs NHE) [21], the sufficiently negative CB potential of $Ag_2S$ indicates that the photoexcited electrons in $Ag_2S$ can reduce $O_2$ to generate $\bullet O_2^-$. On the other hand, the photogenerated holes in the VB of $BiFeO_3$ possess enough oxidation ability to generate $\bullet OH$ ($E^0(OH^-/\bullet OH) = +1.99$ V vs NHE) [74]. Under visible-light irradiation, and in the presence of $H_2O_2$, photocatalytic and Fenton reactions simultaneously take place, and moreover, the two catalytic processes exhibit an important synergistic effect, as schematically shown in Figure 12b. In the photo-Fenton catalytic process, $Fe^{2+}$ on the surface of $BiFeO_3$ can react with $H_2O_2$ to generate $\bullet OH$ and $Fe^{3+}$. Then, $Fe^{3+}$ will be reduced into $Fe^{2+}$ by the photogenerated electrons. In this cyclic reaction, more $\bullet OH$ radicals are being produced, but the consumption of the photogenerated electrons leads to the decreased generation of $\bullet O_2^-$ radicals. This could be the reason that $\bullet OH$ plays an important role in the degradation of the dye during the photo-Fenton catalytic process. The main photo-Fenton reaction process can be briefly described by Equations (3)–(9):
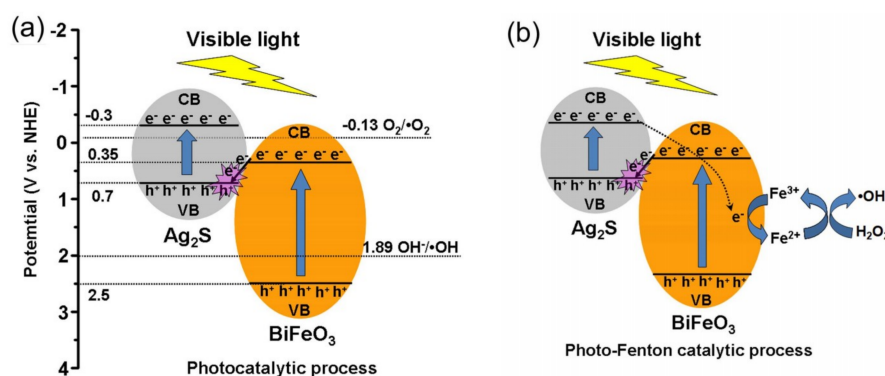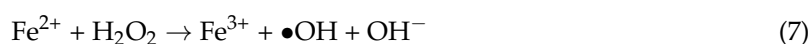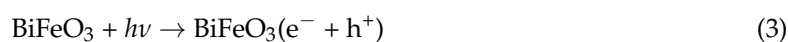
$$BiFeO_3 + h\nu \rightarrow BiFeO_3(e^- + h^+) \tag{3}$$

$$Ag_2S + h\nu \rightarrow Ag_2S\,(e^- + h^+) \tag{4}$$

$$h^+(BiFeO_3) + OH^- \rightarrow \bullet OH \tag{5}$$

$$e^-(Ag_2S) + O_2 \rightarrow \bullet O_2^- \tag{6}$$

$$Fe^{2+} + H_2O_2 \rightarrow Fe^{3+} + \bullet OH + OH^- \tag{7}$$

$$Fe^{3+} + e^-(Ag_2S) \rightarrow Fe^{2+} \tag{8}$$

$$\bullet OH, h^+, \bullet O_2^- + MO \rightarrow degradation\ products \tag{9}$$



**Figure 12.** Schematic illustration of the degradation mechanism of MO over the $Ag_2S/BiFeO_3$ composites. (**a**) The photocatalytic process; (**b**) the photo-Fenton catalytic process.

## 4. Conclusions

A series of Z-scheme $Ag_2S/BiFeO_3$ heterojunction composites have been constructed by assembling $Ag_2S$ nanoparticles on the surface of the $BiFeO_3$ polyhedra. It is demonstrated that the $Ag_2S/BiFeO_3$ composites can be employed as a promising catalyst for the photocatalytic and photo-Fenton catalytic decomposition of MO under visible-light irradiation. Compared to the bare photocatalytic process, the synergistic effect of photo-Fenton catalysis in the presence of $H_2O_2$ leads to a higher degradation efficiency of the dye. The optimum composite sample is observed for 15% $Ag_2S/BiFeO_3$, which photo-Fenton-catalyzes ~97% degradation of MO after 4 h of reaction under the optimal conditions. The enhanced catalytic activity of the Z-scheme $Ag_2S/BiFeO_3$ heterojunction composites can be explained as the result of efficient separation of photoexcited $e^-$-$h^+$ pairs, resulting from the Z-scheme electron transfer.

## References

1. Brown, M.A.; De Vito, S.C. Predicting azo dye toxicity. *Crit. Rev. Environ. Sci. Technol.* **1993**, *23*, 249–324. [CrossRef]

2. de Caprariis, B.; De Filippis, P.; Hernandez, A.D.; Petrucci, E.; Petrullo, A.; Scarsella, M.; Turchi, M. Pyrolysis wastewater treatment by adsorption on biochars produced by poplar biomass. *J. Environ. Manag.* **2017**, *197*, 231–238. [CrossRef] [PubMed]

3. Moreno, R.; San-Martin, M.I.; Escapa, A.; Moran, A. Domestic wastewater treatment in parallel with methane production in a microbial electrolysis cell. *Renew. Energy* **2016**, *93*, 442–448. [CrossRef]

4. Yuan, H.Y.; He, Z. Integrating membrane filtration into bioelectrochemical systems as next generation energy-efficient wastewater treatment technologies for water reclamation: A review. *Bioresour. Technol.* **2015**, *195*, 202–209. [CrossRef] [PubMed]

5. Teh, C.Y.; Budiman, P.M.; Shak, K.P.Y.; Wu, T.Y. Recent advancement of coagulation-flocculation and its application in wastewater treatment. *Ind. Eng. Chem. Res.* **2016**, *55*, 4363–4389. [CrossRef]

6. Zhao, X.X.; Yang, H.; Li, S.H.; Cui, Z.M.; Zhang, C.R. Synthesis and theoretical study of large-sized $Bi_4Ti_3O_{12}$ square nanosheets with high photocatalytic activity. *Mater. Res. Bull.* **2018**, *107*, 180–188. [CrossRef]

7. Xia, Y.M.; He, Z.M.; Yang, W.; Tang, B.; Lu, Y.L.; Hu, K.J.; Su, J.B.; Li, X.P. Effective charge separation in $BiOI/Cu_2O$ composites with enhanced photocatalytic activity. *Mater. Res. Express* **2018**, *5*, 025504. [CrossRef]

8. Chakma, S.; Das, L.; Moholkar, V.S. Dye decolorization with hybrid advanced oxidation processes comprising sonolysis/Fenton-like/photo-ferrioxalate systems: A mechanistic investigation. *Sep. Purif. Technol.* **2015**, *156*, 596–607. [CrossRef]

9. Guin, J.P.; Naik, D.B.; Bhardwaj, Y.K.; Varshney, L. An insight into the effective advanced oxidation process for treatment of simulated textile dye waste water. *RSC Adv.* **2014**, *4*, 39941–39947. [CrossRef]

10. Wang, S.F.; Gao, H.J.; Wei, Y.; Li, Y.W.; Yang, X.H.; Fang, L.M.; Lei, L. Insight into the optical, color, photoluminescence properties, and photocatalytic activity of the N-O and C-O functional groups decorating spinel type magnesium aluminate. *CrystEngComm* **2019**, *21*, 263–277. [CrossRef]

11. Yan, Y.X.; Yang, H.; Zhao, X.X.; Li, R.S.; Wang, X.X. Enhanced photocatalytic activity of surface disorder-engineered $CaTiO_3$. *Mater. Res. Bull.* **2018**, *105*, 286–290. [CrossRef]

12. Yamashita, H.; Mori, K.; Kuwahara, Y.; Kamegawa, T.; Wen, M.C.; Verma, P.; Che, M. Single-site and nano-confined photocatalysts designed in porous materials for environmental uses and solar fuels. *Chem. Soc. Rev.* **2018**, *47*, 8072–8096. [CrossRef] [PubMed]

13. Zhao, W.H.; Wei, Z.Q.; Zhang, L.; Wu, X.J.; Wang, X. Cr doped $SnS_2$ nanoflowers: Preparation, characterization and photocatalytic decolorization. *Mater. Sci. Semicond. Process.* **2018**, *88*, 173–180. [CrossRef]

14. Xia, Y.; He, Z.; Su, J.; Liu, Y.; Tang, B. Fabrication and photocatalytic property of novel $SrTiO_3/Bi_5O_7I$ nanocomposites. *Nanoscale Res. Lett.* **2018**, *13*, 148. [CrossRef] [PubMed]

15. Wang, S.Y.; Yang, H.; Wang, X.X.; Feng, W.J. Surface disorder engineering of flake-like $Bi_2WO_6$ crystals for enhanced photocatalytic activity. *J. Electron. Mater.* **2019**. [CrossRef]

16. He, Y.; Jiang, D.B.; Jiang, D.Y.; Chen, J.; Zhang, Y.X. Evaluation of $MnO_2$-templated iron oxide-coated diatomites for their catalytic performance in heterogeneous photo Fenton-like system. *J. Hazard. Mater.* **2018**, *344*, 230–240. [CrossRef] [PubMed]

17. Shiraz, A.D.; Takdastan, A.; Borghei, S.M. Photo-Fenton like degradation of catechol using persulfate activated by UV and ferrous ions: Influencing operational parameters and feasibility studies. *J. Mol. Liq.* **2018**, *249*, 463–369. [CrossRef]

18. Guo, X.J.; Wang, K.B.; Li, D.; Qin, J.B. Heterogeneous photo-Fenton processes using graphite carbon coating hollow $CuFe_2O_4$ spheres for the degradation of methylene blue. *Appl. Surf. Sci.* **2017**, *420*, 792–801. [CrossRef]

19. Valero-Luna, C.; Palomares-Sanchez, S.A.; Ruiz, F. Catalytic activity of the barium hexaferrite with $H_2O_2$/visible light irradiation for degradation of methylene blue. *Catal. Today* **2016**, *266*, 110–119. [CrossRef]

20. Rabbani, M.; Rahimi, R.; Ghadi, H.F. Photocatalytic application of $BiFeO_3$ synthesized via a facile microwave-assisted solution combustion method. *J. Sol-Gel Sci. Technol.* **2018**, *87*, 340–346. [CrossRef]

21. Di, L.J.; Yang, H.; Xian, T.; Chen, X.J. Enhanced photocatalytic activity of NaBH4 reduced BiFeO3 nanoparticles for rhodamine B decolorization. *Materials* **2017**, *10*, 1118. [CrossRef]

22. Basith, M.A.; Yesmin, N.; Hossain, R. Low temperature synthesis of $BiFeO_3$ nanoparticles with enhanced magnetization and promising photocatalytic performance in dye degradation and hydrogen evolution. *RSC Adv.* **2018**, *8*, 29613–29627. [CrossRef]

23. Lam, S.M.; Sin, J.C.; Mohamed, A.R. A newly emerging visible light-responsive $BiFeO_3$ perovskite for photocatalytic applications: A mini review. *Mater. Res. Bull.* **2017**, *90*, 15–30. [CrossRef]

24. Guo, Y.S.; Pu, Y.P.; Cui, Y.F.; Hui, C.Y.; Wan, J.; Cui, C.W. A simple method using citric acid as the template agent to improve photocatalytic performance of $BiFeO_3$ nanoparticles. *Mater. Lett.* **2017**, *196*, 57–60. [CrossRef]

25. Bharathkumar, S.; Sakar, M.; Balakumar, S. Experimental evidence for the carrier transportation enhanced visible light driven photocatalytic process in bismuth ferrite ($BiFeO_3$) one-dimensional fiber nanostructures. *J. Phys. Chem. C* **2016**, *120*, 18811–18821. [CrossRef]

26. Wang, X.F.; Mao, W.W.; Zhang, Q.X.; Wang, Q.; Zhu, Y.Y.; Zhang, J.; Yang, T.; Yang, J.P.; Li, X.A.; Huang, W. PVP assisted hydrothermal fabrication and morphology-controllable fabrication of $BiFeO_3$ uniform nanostructures with enhanced photocatalytic activities. *J. Alloys Compd.* **2016**, *677*, 288–293. [CrossRef]

27. Bharathkumar, S.; Sakar, M.; Vinod, R.K.; Balakumar, S. Versatility of electrospinning in the fabrication of fibrous mat and mesh nanostructures of bismuth ferrite ($BiFeO_3$) and their magnetic and photocatalytic activities. *Phys. Chem. Chem. Phys.* **2015**, *17*, 17745–17754. [CrossRef] [PubMed]

28. Jia, Y.F.; Wu, C.J.; Kim, D.H.; Lee, B.W.; Rhee, S.J.; Park, Y.C.; Kim, C.S.; Wang, Q.J.; Liu, C.L. Nitrogen doped $BiFeO_3$ with enhanced magnetic properties and photo-Fenton catalytic activity for degradation of bisphenol A under visible light. *Chem. Eng. J.* **2018**, *337*, 709–721. [CrossRef]

29. Soltani, T.; Lee, B.K. Enhanced formation of sulfate radicals by metal-doped $BiFeO_3$ under visible light for improving photo-Fenton catalytic degradation of 2-chlorophenol. *Chem. Eng. J.* **2017**, *313*, 1258–1268. [CrossRef]

30. Yu, W.L.; Zhang, J.F.; Peng, T.Y. New insight into the enhanced photocatalytic activity of N-, C- and S-doped ZnO photocatalysts. *Appl. Catal. B-Environ.* **2016**, *181*, 220–227. [CrossRef]

31. Lee, J.E.; Bera, S.; Choi, Y.S.; Lee, W.I. Size-dependent plasmonic effects of M and $M@SiO_2$ (M = Au or Ag) deposited on $TiO_2$ in photocatalytic oxidation reactions. *Appl. Catal. B-Environ.* **2017**, *214*, 15–22. [CrossRef]

32. Wang, X.X.; Bai, X.L.; Pang, Z.Y.; Yang, H.; Qi, Y.P.; Wen, X.L. Surface-enhanced Raman scattering effect of a composite structure with gold nano-cubes and gold film separated by Polymethylmethacrylate film. *Acta Phys. Sin.* **2019**, *68*, 037301.

33. Zheng, C.X.; Yang, H.; Cui, Z.M.; Zhang, H.M.; Wang, X.X. A novel $Bi_4Ti_3O_{12}/Ag_3PO_4$ heterojunction photocatalyst with enhanced photocatalytic performance. *Nanoscale Res. Lett.* **2017**, *12*, 608. [CrossRef]

34. Zeng, Y.; Chen, X.F.; Yi, Z.; Yi, Y.G.; Xu, X.B. Fabrication of p-n heterostructure ZnO/Si moth-eye structures: Antireflection, enhanced charge separation and photocatalytic properties. *Appl. Surf. Sci.* **2018**, *441*, 40–48. [CrossRef]

35. Tang, J.H.; Wang, R.X.; Liu, M.Y.; Zhang, Z.H.; Song, Y.T.; Xue, S.; Zhao, Z.G.; Dionysiou, D.D. Construction of novel Z-scheme $Ag/FeTiO_3/Ag/BiFeO_3$ photocatalyst with enhanced visible-light-driven photocatalytic performance for degradation of norfloxacin. *Chem. Eng. J.* **2018**, *351*, 1056–1066. [CrossRef]

36. Li, H.F.; Quan, X.; Chen, S.; Yu, H.T. Ferroelectric-enhanced Z-schematic electron transfer in $BiVO_4$-$BiFeO_3$-$CuInS_2$ for efficient photocatalytic pollutant degradation. *Appl. Catal. B Environ.* **2017**, *209*, 591–599. [CrossRef]

37. Di, L.J.; Yang, H.; Xian, T.; Chen, X.J. Facile synthesis and enhanced visible-light photocatalytic activity of novel p-Ag$_3$PO$_4$/n-BiFeO$_3$ heterojunction composites for dye degradation. *Nanoscale. Res. Lett.* **2018**, *13*, 257. [CrossRef] [PubMed]

38. Fernando, K.A.S.; Sahu, S.P.; Liu, Y.; Lewis, W.K.; Guliants, E.; Jafariyan, A.; Wang, P.; Bunker, C.E.; Sun, Y.P. Carbon quantum dots and applications in photocatalytic energy conversion. *ACS Appl. Mater. Interfaces* **2015**, *7*, 8363–8376. [CrossRef] [PubMed]

39. Cen, C.L.; Lin, H.; Huang, J.; Liang, C.P.; Chen, X.F.; Tang, Y.J.; Yi, Z.; Ye, X.; Liu, J.W.; Yi, Y.G.; et al. A tunable plasmonic refractive index sensor with nanoring-strip graphene arrays. *Sensors* **2018**, *18*, 4489. [CrossRef]

40. Jiang, J.L.; He, X.X.; Du, J.F.; Pang, X.J.; Yang, H.; Wei, Z.Q. In-situ fabrication of graphene-nickel matrix composites. *Mater. Lett.* **2018**, *220*, 178–181. [CrossRef]

41. Yang, Y.N.; Xia, L.; Zhang, T.; Shi, B.; Huang, L.N.; Zhong, B.; Zhang, X.Y.; Wang, H.T.; Zhang, J.; Wen, G.W. Fe$_3$O$_4$@LAS/RGO composites with a multiple transmission-absorption mechanism and enhanced electromagnetic wave absorption performance. *Chem. Eng. J.* **2018**, *352*, 510–518. [CrossRef]

42. Liang, C.P.; Niu, G.; Chen, X.F.; Zhou, Z.G.; Yi, Z.; Ye, X.; Duan, T.; Yi, Y.; Xiao, S.Y. Tunable triple-band graphene refractive index sensor with good angle-polarization tolerance. *Opt. Commun.* **2019**, *436*, 57–62. [CrossRef]

43. Lin, H.; Ye, X.; Chen, X.F.; Zhou, Z.G.; Yi, Z.; Niu, G.; Yi, Y.G.; Hua, Y.T.; Hua, J.G.; Xiao, S.Y. Plasmonic absorption enhancement in grapheme circular and Elliptical disk arrays. *Mater. Res. Express* **2019**, *6*, 045807. [CrossRef]

44. Wang, X.X.; Tong, H.; Pang, Z.Y.; Zhu, J.K.; Wu, X.X.; Yang, H.; Qi, Y.P. Theoretical realization of three-dimensional nanolattice structure fabrication based on high-order waveguide-mode interference and sample rotation. *Opt. Quant. Electron.* **2019**, *51*, 38. [CrossRef]

45. Pang, Z.Y.; Tong, H.; Wu, X.X.; Zhu, J.K.; Wang, X.X.; Yang, H.; Qi, Y.P. Theoretical study of multiexposure zeroth-order waveguide mode interference lithography. *Opt. Quant. Electron.* **2018**, *50*, 335. [CrossRef]

46. Wang, X.X.; Pang, Z.Y.; Tong, H.; Wu, X.X.; Bai, X.L.; Yang, H.; Wen, X.L.; Qi, Y.P. Theoretical investigation of subwavelength structure fabrication based on multi-exposure surface plasmon interference lithography. *Results Phys.* **2019**, *12*, 732–737. [CrossRef]

47. Wang, X.X.; Bai, X.L.; Pang, Z.Y.; Yang, H.; Qi, Y.P. Investigation of surface plasmons in Kretschmann structure loaded with a silver nano-cube. *Results Phys.* **2019**, *12*, 1866–1870. [CrossRef]

48. Xia, L.; Zhang, X.Y.; Yang, Y.N.; Zhang, J.; Zhong, B.; Zhang, T.; Wang, H.T. Enhanced electromagnetic wave absorption properties of laminated SiCNW-Cf/lithium-aluminum-silicate (LAS) composites. *J. Alloys Compd.* **2018**, *748*, 154–162. [CrossRef]

49. Sadovnikov, S.I.; Vovkotrub, E.G. Thermal stability of nanoparticle size and phase composition of nanostructured Ag$_2$S silver sulfide. *J. Alloys Compd.* **2018**, *766*, 140–148. [CrossRef]

50. Cen, C.L.; Liu, L.; Zhang, Y.B.; Chen, X.F.; Zhou, Z.G.; Yi, Z.; Ye, X.; Tang, Y.J.; Yi, Y.G.; Xiao, S.Y. Tunable absorption enhancement in periodic elliptical hollow graphene arrays. *Opt. Mater. Express* **2019**, *9*, 706–716. [CrossRef]

51. Yi, Z.; Lin, H.; Niu, G.; Chen, X.F.; Zhou, Z.G.; Ye, X.; Duan, T.; Yi, Y.; Tang, Y.J.; Yi, Y.G. Graphene-based tunable triple-band plasmonic perfect metamaterial absorber with good angle-polarization-tolerance. *Results Phys.* **2019**. [CrossRef]

52. Di, L.J.; Yang, H.; Xian, T.; Chen, X.J. Construction of Z-scheme g-C$_3$N$_4$/CNT/Bi$_2$Fe$_4$O$_9$ composites with improved simulated-sunlight photocatalytic activity for the dye degradation. *Micromachines* **2018**, *9*, 613. [CrossRef] [PubMed]

53. Isari, A.A.; Payan, A.; Fattahi, M.; Jorfi, S.; Kakavandi, B. Photocatalytic degradation of rhodamine B and real textile wastewater using Fe-doped TiO$_2$ anchored on reduced grapheme oxide (Fe-TiO$_2$/rGO): Characterization and feasibility, mechanism and pathway studies. *Appl. Surf. Sci.* **2018**, *462*, 549–564. [CrossRef]

54. Khanchandani, S.; Srivastava, P.K.; Kumar, S.; Ghosh, S.; Ganguli, A.K. Band gap engineering of ZnO using core/shell morphology with environmentally benign Ag$_2$S sensitizer for efficient light harvesting and enhanced visible-light photocatalysis. *Inorg. Chem.* **2014**, *53*, 8902–8912. [CrossRef] [PubMed]

55. Peng, Y.; Han, G.; Wang, D.; Wang, K.X.; Guo, Z.N.; Yang, J.J.; Yuan, W.X. Improved H$_2$ evolution under visible light in heterostructured SiC/CdS photocatalyst: Effect of lattice match. *Int. J. Hydrogen Energy* **2017**, *42*, 14409–14417. [CrossRef]

56. Zhao, X.X.; Yang, H.; Cui, Z.M.; Wang, X.X.; Yi, Z. Growth process and CQDs-modified Bi$_4$Ti$_3$O$_{12}$ square plates with enhanced photocatalytic performance. *Micromachines* **2019**, *10*, 66. [CrossRef] [PubMed]

57. Yuan, L.; Lu, S.W.; Yang, F.; Wang, Y.S.; Jia, Y.F.; Kadhim, M.S.; Yu, Y.M.; Zhang, Y.; Zhao, Y. A facile room-temperature synthesis of three-dimensional coral-like Ag$_2$S nanostructure with enhanced photocatalytic activity. *J. Mater. Sci.* **2019**, *54*, 3174–3186. [CrossRef]

58. Jiang, W.; Wu, Z.M.; Yue, X.N.; Yuan, S.J.; Lu, H.F.; Liang, B. Photocatalytic performance of Ag$_2$S under irradiation with visible and near-infrared light and its mechanism of degradation. *RSC Adv.* **2015**, *5*, 24064–24071. [CrossRef]

59. Chen, D.; Wei, L.; Wang, D.; Chen, Y.X.; Tian, Y.F.; Yan, S.S.; Mei, L.M.; Jiao, J. Ag$_2$S/ZnO core-shell nanoheterojunction for a self-powered solid-state photodetector with wide spectral response. *J. Alloys Compd.* **2018**, *735*, 2491–2496. [CrossRef]

60. Zhao, X.X.; Yang, H.; Li, R.S.; Cui, Z.M.; Liu, X.Q. Synthesis of heterojunction photocatalysts composed of Ag$_2$S quantum dots combined with Bi$_4$Ti$_3$O$_{12}$ nanosheets for the degradation of dyes. *Environ. Sci. Pollut. Res. Int.* **2019**, *26*, 5524–5538. [CrossRef] [PubMed]

61. Abdullah, H.; Kuo, D.H. Facile synthesis of n-type (AgIn)$_x$Zn$_{2(1-x)}$S$_2$/p-type Ag$_2$S nanocomposite for visible light photocatalytic reduction to detoxify hexavalent chromium. *ACS Appl. Mater. Interfaces* **2015**, *7*, 26941–26951. [CrossRef] [PubMed]

62. Barrocas, B.; Entradas, T.J.; Nunes, C.D.; Monteiro, O.C. Titanate nanofibers sensitized with ZnS and Ag$_2$S nanoparticles as novel photocatalysts for phenol removal. *Appl. Catal. B Environ.* **2017**, *218*, 709–720. [CrossRef]

63. Zhu, X.L.; Wei, Z.Q.; Zhao, W.H.; Zhang, X.D.; Zhang, L.; Wang, X. Microstructure and electrochemical properties of ZnMn$_2$O$_4$ nanopowder synthesized using different surfactants. *J. Electron. Mater.* **2018**, *47*, 6428–6436. [CrossRef]

64. Yan, Y.X.; Yang, H.; Zhao, X.X.; Zhang, H.M.; Jiang, J.L. A hydrothermal route to the synthesis of CaTiO$_3$ nanocuboids using P25 as the titanium source. *J. Electron. Mater.* **2018**, *47*, 3045–3050. [CrossRef]

65. Andersen, T.; Haugen, H.K.; Hotop, H. Binding energies in atomic negative ions: III. *J. Phys. Chem. Ref. Data* **1999**, *28*, 1511. [CrossRef]

66. Ye, Y.C.; Yang, H.; Zhang, H.M.; Jiang, J.L. A promising Ag$_2$CrO$_4$/LaFeO$_3$ heterojunction photocatalyst applied to photo-Fenton degradation of RhB. *Environ. Technol.* **2018**. [CrossRef] [PubMed]

67. Pooladi, M.; Shokrollahi, H.; Lavasani, S.A.N.H.; Yang, H. Investigation of the structural, magnetic and dielectric properties of Mn-doped Bi2Fe$_4$O$_9$ produced by reverse chemical co-precipitation. *Mater. Chem. Phys.* **2019**. [CrossRef]

68. Reddy, D.A.; Ma, R.; Choi, M.Y.; Kim, T.K. Reduced graphene oxide wrapped ZnS-Ag$_2$S ternary compositessynthesized via hydrothermal method: Applications in photocatalystdegradation of organic pollutants. *Appl. Surf. Sci.* **2015**, *324*, 725–735. [CrossRef]

69. Li, X.; Chen, X.F.; Yi, Z.; Zhou, Z.G.; Tang, Y.J.; Yi, Y.G. Fabriction of ZnO nanorods with strong UV absorption and different hydrophobicity on foamed nickel under different hydrothermal conditions. *Micromachines* **2019**, *10*, 164. [CrossRef]

70. Zheng, C.X.; Yang, H. Assembly of Ag$_3$PO$_4$ nanoparticles on rose flower-like Bi$_2$WO$_6$ hierarchical architectures for achieving high photocatalytic performance. *J. Mater. Sci.-Mater. Electron.* **2018**, *29*, 9291–9300. [CrossRef]

71. Wang, S.F.; Gao, H.J.; Fang, L.M.; Wei, Y.; Li, Y.W.; Lei, L. Synthesis and characterization of BaAl$_2$O$_4$ catalyst and its photocatalytic activity towards degradation of methylene blue dye. *Z. Phys. Chem.* **2019**. [CrossRef]

72. Zhao, X.X.; Yang, H.; Zhang, H.M.; Cui, Z.M.; Feng, W.J. Surface-disorder-engineering-induced enhancement in the photocatalytic activity of Bi$_4$Ti$_3$O$_{12}$ nanosheets. *Desalin. Water Treat.* **2019**. [CrossRef]

73. Ning, X.B.; Ge, S.S.; Wang, X.T.; Li, H.; Li, X.R.; Liu, X.Q.; Huang, Y.L. Preparation and photocathodic protection property of Ag$_2$S-TiO$_2$ composites. *J. Environ. Chem. Eng.* **2018**, *6*, 311–324.

74. Xia, Y.M.; He, Z.M.; Lu, Y.L.; Tang, B.; Sun, S.P.; Su, J.B.; Li, X.P. Fabrication and photocatalytic property of magnetic SrTiO$_3$/NiFe$_2$O$_4$ heterojunction nanocomposites. *RSC Adv.* **2018**, *8*, 5441–5450. [CrossRef]